nature communications

Article

https://doi.org/10.1038/s41467-026-70289-3

Directional dynamics in the entorhinal cortex of male mice driven by behavioral constraints

Received: 11 May 2025

Accepted: 24 February 2026

Published online: 09 March 2026

Check for updates

Ruojin Liu[1,2,3,7], Jun Hao[2,3,6,7], Xiang Zhang[2,3], Shidan Wen[2,3], Youran Yang[1,2,3], Haiqian Cai[1,2,3], Kai Gao[1,2,3], Emilio Kropff[4,8] ✉ & Chenglin Miao[1,2,3,5,8] ✉

The medial entorhinal cortex of rodents contains a variety of functionally-defined cell types, including grid and head direction cells. While evidence indicates that functional types are not associated with clear molecular footprints, the factors that define them remain unclear. By comparing neural recordings in male mice exploring the same environment either freely or head-fixed to an autonomous-driving cart, we here show that, for a substantial portion of neurons, the head direction functional identity is dynamic, likely emerging through self-organization. Approximately half of free-foraging head direction cells reversibly lost their tuning during assisted navigation, while other neurons gained directional tuning, especially in environments enriched with sensory cues. This adaptive process is experience-dependent, progressively sharpening and stabilizing directional representations, while also integrating a spatial component. Our findings reveal a remarkable flexibility of entorhinal representations, demonstrating their capacity to reorganize and adapt based on how animals interact with their environment.

The medial entorhinal cortex (mEC) of rodents simultaneously encodes multiple variables related to spatial navigation through distinct, functionally-defined cell types, such as grid and head direction (HD) cells[1–4]. Although the mEC contains several anatomically defined cell classes with distinctive electrophysiological properties, functional and anatomical classifications do not map neatly onto one another[5–7]. Consequently, the factors determining the functional identity of neurons in the mEC—potentially involving hard-wiring or self-organization—remain an open question. Plasticity has so far shown to have an influence on tuning functions of several cell types, but not on their functional identity[8–14].

Many highly interconnected brain areas represent direction through HD functionally-defined cells[15]. Vestibular, motor, and multimodal information are thought to be integrated by sub-cortical pathways, producing a robust representation sustained by attractor dynamics in the anterior-dorsal thalamic nucleus[16]. This pathway is required for entorhinal grid cells to express their hexagonal maps[17]. Recent evidence suggests the possibility of a differentiated cortical pathway that, while not independent from subcortical circuits, is more focused on sensory information[18,19]. This duality might be expressed in the mEC, where a distinction between theta modulated and non-modulated HD cells has been made, as only the latter modify their preferred direction in an environment as a consequence of sudden contextual changes[20].

Passively transporting animals in a cart has proven useful for investigating the mechanisms underlying HD representations across

[1]Peking-Tsinghua Center for Life Sciences, Beijing, China. [2]PKU-IDG/McGovern Institute for Brain Research, Peking university, Beijing, China. [3]State Key Laboratory of Membrane Biology, School of Life Science, Peking university, Beijing, China. [4]Leloir Institute/IIBBA-CONICET, Buenos Aires, Argentina. [5]Chinese Institute for Brain Research (CIBR), Beijing, China. [6]Present address: School of Life Sciences, Westlake University, Hangzhou, China. [7]These authors contributed equally: Ruojin Liu, Jun Hao. [8]These authors jointly supervised this work: Emilio Kropff, Chenglin Miao. ✉e-mail: ekropff@leloir.org.ar; chenglin.miao@pku.edu.cn

the brain[21–24]. In the mEC, passive transport disrupts grid maps, suggesting that motor engagement is essential for their proper implementation[25,26]. Interestingly, passive transport has also been reported to enhance the directionality of some grid cells, but not conjunctive cells, while keeping HD cells mostly spared despite some mild loss in directional selectivity[25]. These contrasting effects may either represent specific deficits in distinct cell subpopulations or, alternatively, reflect a broader reconfiguration of entorhinal HD representations, a possibility that remains unaddressed. Here, we developed assisted navigation—similar to passive transport, but with tighter control over the two-dimensional trajectory, achieved by head-fixing mice to an autonomous-driving cart. Leveraging two-photon calcium imaging, this approach enabled us to comprehensively examine how behavioral constraints re-organize functionally-defined HD cells within the wider entorhinal network.

Results

Reconfiguration of directional codes

To study entorhinal representations during free and assisted navigation, we injected the adeno-associated virus AAV-hSyn-GCamMP6f in the entorhinal cortex of 12 mice. In each animal we implanted a prism that allowed calcium imaging through a two-photon miniaturized microscope (Fig. 1a, b and Supplementary Fig. 1a). We selected a total of 11,818 cells (between 240 and 2245 per mouse) with high signal-to-noise ratio and extracted events through deconvolution and binarization of calcium activity raw traces using standard methods[27] (Fig. 1c, d). A comparison of the autocorrelation decay of deconvolved calcium events and head direction confirmed that our neural recordings had sufficient temporal resolution to capture HD variations during both free and assisted navigation sessions (Supplementary Fig. 2a, b).

We first investigated the head-direction code during navigation in a 80 cm side square environment containing visual and odor cues. In this arena, mice had two sessions of free exploration separated by a session of assisted navigation, with 5 min resting in-between sessions (Fig. 1e). For assisted navigation, mice were head-fixed to an autonomous-driving cart that changed speed and direction at intervals between 100 and 1500 ms in a pseudo-random-walk fashion (Supplementary Movie 1). Ultrasound sensors were used to prevent the car from bumping against walls. Mean coverage of the arena (free: 91%, assisted: 93%) and mean speed (free: 9.0 cm s^{-1}, assisted: 8.5 cm s^{-1}) were comparable across conditions (Supplementary Fig. 2c–e).

For each of the 4528 cells recorded in this experiment (8 mice in 11 experimental days), we obtained head-direction (HD) tuning curves and characterized them by their mean vector length (MVL), angular information and stability (Fig. 1f). Previous work on passive transport inside a plexiglass cage pointed to a mild decay in selectivity of HD cells that did not alter their functional identity[25], but did not address HD modulation in the general population, which we examined. Surprisingly, we found that during assisted navigation, average HD selectivity increased both in terms of mean vector length and HD information rate (Fig. 1f). This increase in HD selectivity was not due to sparse sporadic activation, since also stability, obtained as the Pearson correlation between HD maps corresponding to consequtive halves of the same session, increased during assisted navigation. Similar conclusions were obtained when using only one experimental day per animal (Supplementary Fig. 3a, b), as well as when downsampling data to match either speed (Supplementary Fig. 3c–e) or angular velocity (Supplementary Fig. 3f–i) distributions of free and assisted sessions or considering only the center-most part of the arena (Supplementary Fig. 4). These results point to a reconfiguration of HD representations across navigation modalities, resulting in an overall increase rather than an impairment in directional selectivity in the mEC during assisted navigation.

To characterize neural activity across conditions, we next classified individual neurons as HD cells if their MVL was higher than the 99th percentile of the distribution obtained from a shuffling procedure pooling all data from the first free navigation session of each experiment (cutoff: 0.44; pool of 1000 shuffles for each cell; Supplementary Figs. 5–6a). We identified three groups of HD cells, which did not cluster anatomically (Supplementary Fig. 1b–d). HD_F cells passed the criterion during the first free navigation session (179 cells or 3.9%) but not during the assisted session (Fig. 1g, h). Conversely, HD_A cells passed the criterion only during the assisted session, adding up to a higher proportion of the overall population (482 cells or 10.6%). A third group of cells, HD_I (where *I* stands for *invariant*; see below), passed the classification criteria in both session (144 cells or 3.2%). This group, compared to HD_A and HD_F, exhibited lower mean acitivity levels, together with higher HD selectivity and stability across sessions (Fig. 1i and Supplementary Fig. 6b). The proportion of these cells was significantly larger than expected with a false positive probability of 0.01, given the classification criterion based on the 99th percentile of the shuffled distribution (binomial test $p < 10^{-50}$ for all HD subpopulations). The tuning patterns of these cells remained stable across sessions and consecutive days (Supplementary Fig. 6c–e), further reinforcing the reliability of the directional tuning.

We next asked if HD_I cells had the same preferred direction or remapped across conditions. For each cell, we quantified remapping by the Pearson correlation between the HD maps corresponding to different sessions (Fig. 1i). We found that HD_I cells had the highest level of correlation across sessions, and it was not significantly different when comparing sessions with matched or non-matched navigation modalities. HD_F cells, in contrast, had a significantly lower correlation when comparing sessions across modalities, indicative of remapping.

To investigate the reconfiguration of directional representations from a population coding perspective, we used a Bayesian decoder within a cross-validation framework (Fig. 1j). We trained and tested the decoder with data coming from either matched or non-matched navigation modalities. We observed that when datasets were matched, the same population of cells decoded direction better during assisted navigation than during free foraging (Fig. 1k). In addition, the decoded error was smaller for matched than non-matched datasets, further demonstrating the modulation of HD representations by navigation modality.

Put together, these results suggest that behavior constraints drive a reconfiguration of HD functional identity in the entorhinal cortex. Speciallized codes, represented by HD_A and HD_F cells, are navigation-modality specific, while HD_I cells implement an invariant directional code. Overall stronger directional modulation during assisted navigation might reflect an adaptation to absent or unreliable self-motion inputs.

Population code reconfiguration

Given that HD cells in some brain areas are thought to follow an attractor dynamic[16,28–31], we next asked whether the loss of directionality in HD_F cells during assisted navigation could result from poor anchoring within an otherwise coherent population activity. If this were the case, temporal correlations between pairs of HD_F cells with similar preferred direction should be preserved in the assisted session despite the loss in selectivity[16,32,33]. We divided free and assisted sessions into two halves and used one half to sort HD cells according to directional preference (first half of free session for HD_F and HD_I, second half of assisted session for HD_A; Fig. 2a). We used the remaining data to assess the presence of a diagonal band in the cell-pair correlation matrix, quantifying it by calculating the ratio of in-diagonal to off-diagonal values. For HD_F and HD_A we found that this ratio was higher in session halves that matched the modality used for cell sorting, and was not different from 1 for the non-matched modality, indicating a complete loss of cell-pair correlation structure (Fig. 2b, c). In contrast, for HD_I cells the diagonal was preserved: the ratio was higher than 1 and not different across sessions.

https://doi.org/10.1038/s41467-026-70289-3

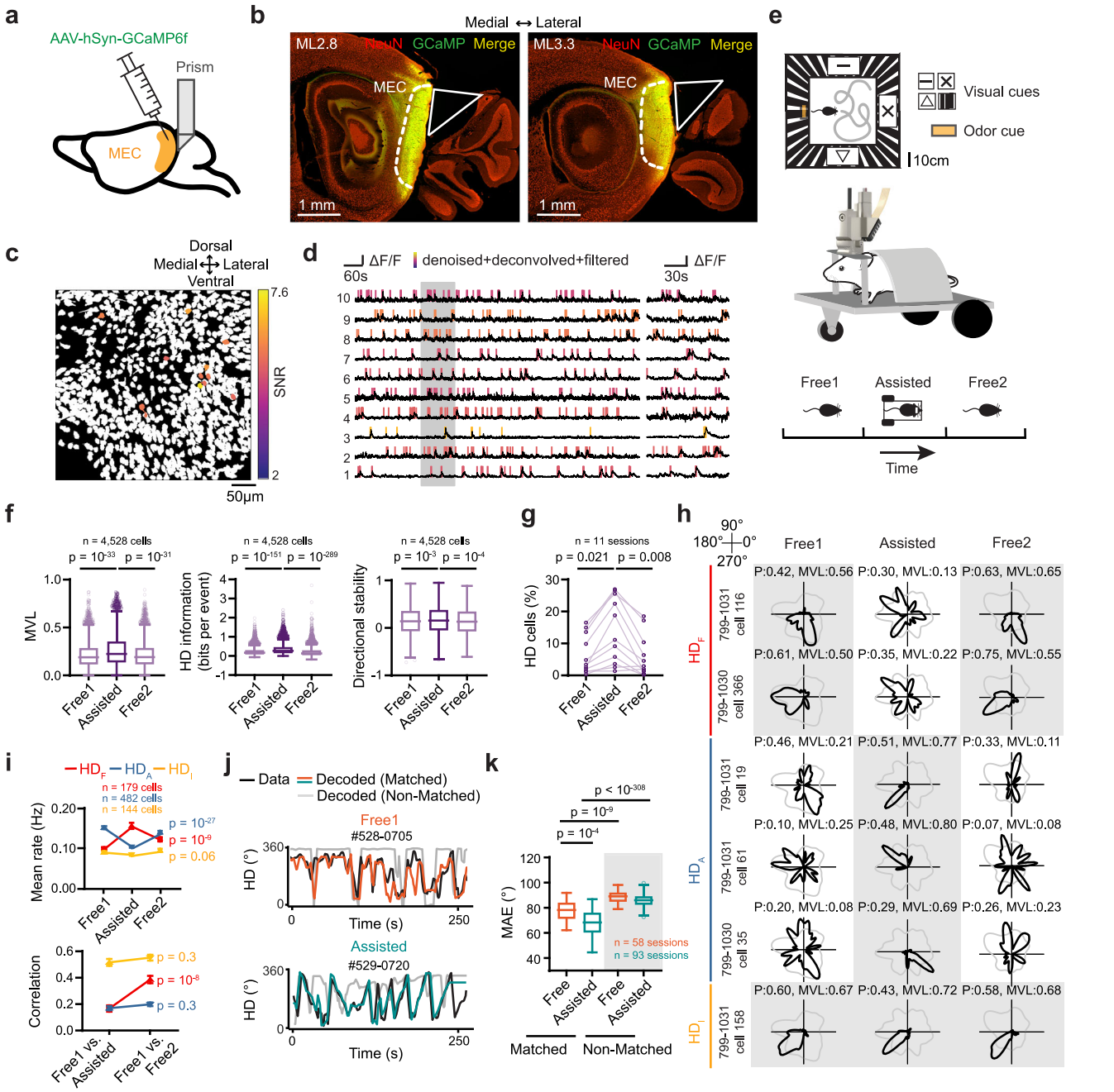


Fig. 1 | Reconfiguration of directional codes during assisted navigation. **a** Schematics of local injection of AAV-GCaMP6f and calcium imaging in MEC. **b** Representative examples of sagittal brain slices from one mouse (red: NeuN; green: GCaMP; yellow: merge; white lines: prism; ML medio-lateral coordinate; $n = 12$ mice in this study). **c** Representative examples of maximum intensity projection and neurons (color-code: signal-to-noise ratio). **d** Left: Calcium traces (normalized ΔF/F; black traces) and filtered, deconvolved signals (colored vertical bars) for examples in (**c**) (same color-code). Right: 105 s excerpt (gray area). **e** Schematics of sensory cues in the arena (top), the assisted navigation setup (middle) and sessions spaced by 5 min resting periods (bottom). Mouse schematic from scidraw.io[70]. **f** Distribution across cells of average MVL, HD information and stability for all recorded cells (Kruskal-Wallis tests $p < 0.0001$ in all cases; MVL: $H = 193.5$, HD information: $H = 1413$, stability: $H = 20.70$; p-values: Dunn's tests). **g** Distribution across sessions of the proportion of cells classified as HD for all sessions (two-tailed Friedman test $S = 10.19$, $p = 0.004$; p-values: Dunn's tests). **h** Representative examples (one cell per row; HD types indicated) of HD rate maps (black) and directional behavior (gray) across sessions, indicating MVL and peak event rate in Hz (P). Gray area: MVL above classification criterion. **i** For different HD types (color-coded), distribution across cells of mean event rate (top) and cross-session angular correlation (bottom) (mean ± s.e.m.; p-values: within HD type Kruskal-Wallis or two-tailed Wilcoxon tests). **j** Representative examples during free (top) and assisted (bottom) sessions of HD (black) and decoded HD using cross-validation training with data from either matching (color) or non-matching (gray) navigation modalities. **k** Distribution of Mean Absolute Error across sessions (color-code as in (**j**); p-values: two-tailed Kolmogorov–Smirnov tests). Speciallized directional codes show a reconfiguration during assisted navigation, with cells either maintaining, losing or acquiring HD tuning across different navigational modalities. For all panels and Figures, boxes: i.q.r., whiskers: ±1.5×i.q.r., where i.q.r. is the interquartile range. Source data are provided as a Source Data file.

https://doi.org/10.1038/s41467-026-70289-3

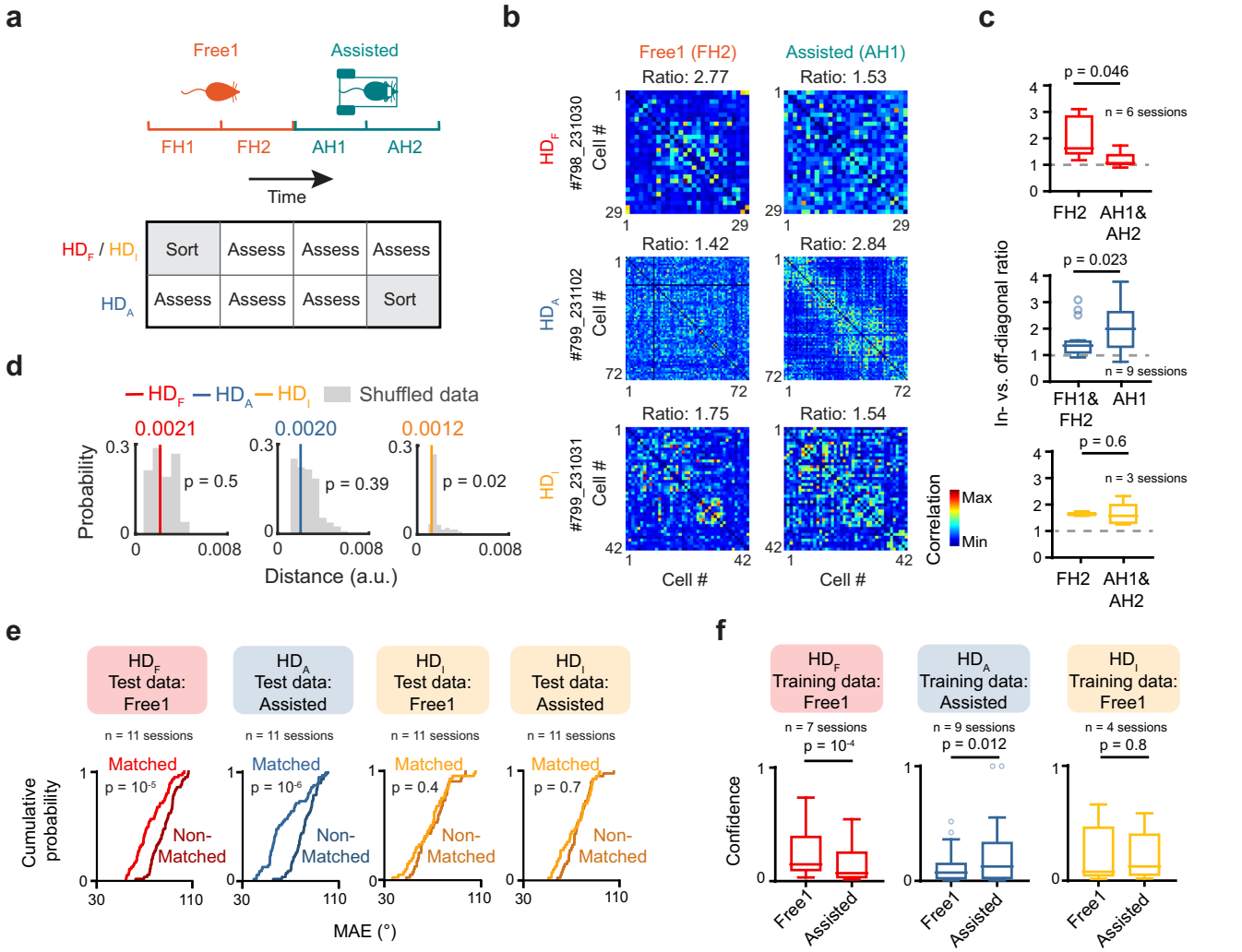


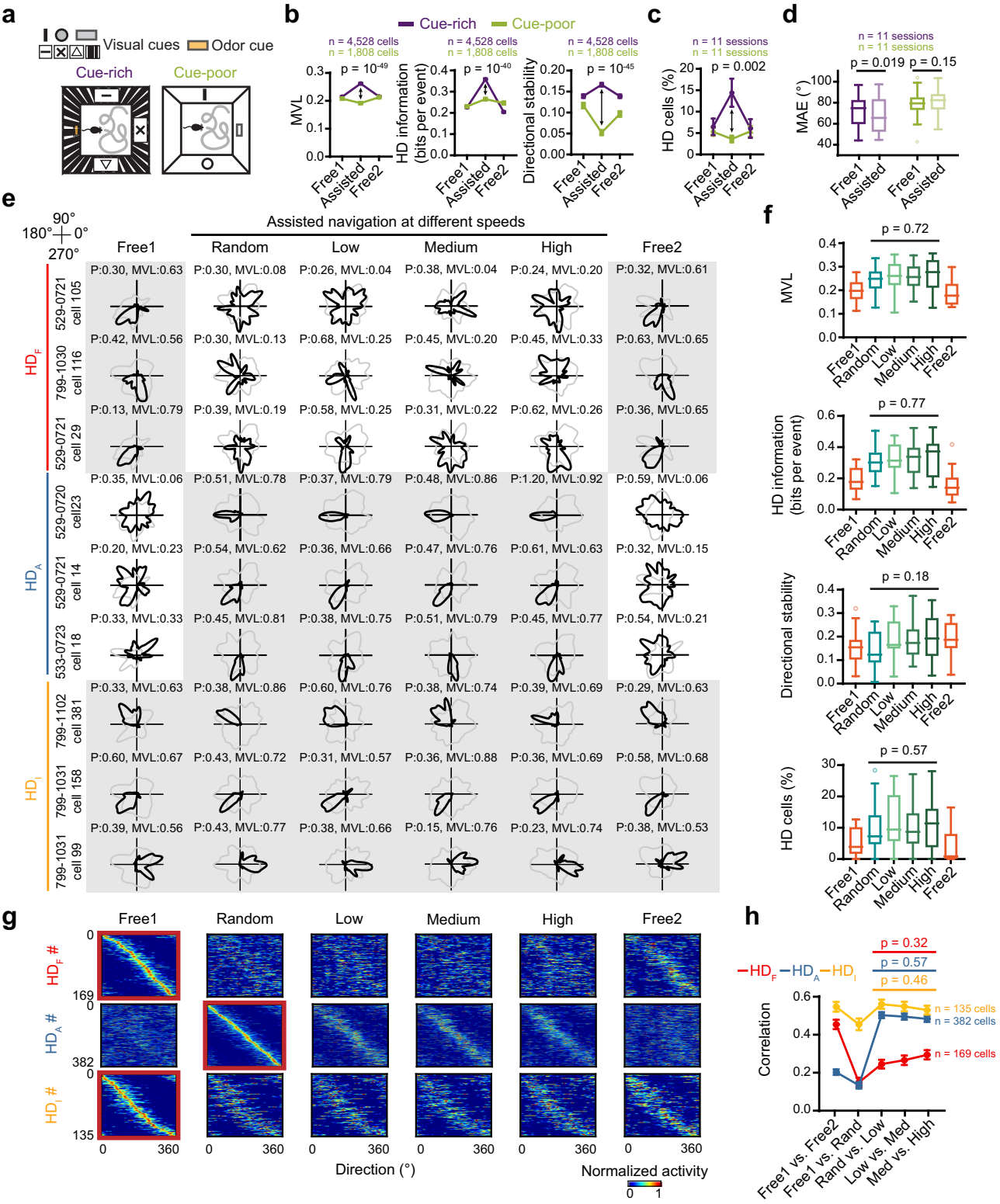
Fig. 2 | Reconfiguration of population activity patterns in HD_A and HD_F cells. **a** Scheme of session halves used to sort cells or assess the presence of a diagonal band in the cell-pair correlation matrix. **b** Representative examples of cell-pair correlation matrices across HD types (rows) and sessions (columns). Ratio of in- to off-diagonal values indicated. **c** Distribution of ratio across all such matrices. All groups above 1 except for HD_F and HD_A in the session not used for sorting (Kruskal-Wallis tests against a value of 1 for each HD type; HD_F: $H = 12.26$, $p = 0.0022$; HD_A: $H = 7.352$, $p = 0.0253$; HD_I: $H = 9.533$, $p = 0.0019$; Dunn's multiple comparison tests $p < 0.02$ for all comparisons except HD_F in the assisted session, $p = 0.15$, and HD_A in the free session, $p = 0.075$), with a significantly lower ratio compared to the other session (two-tailed Kolmogorov–Smirnov tests for differences in ratio across conditions as indicated: HD_F, $D = 0.67$, $p = 0.046$; HD_A, $D = 0.61$, $p = 0.023$; HD_I, $D = 0.50$, $p = 0.6$). **d** Frobenious mean distance between matrices for free vs. assisted sessions (color line, value indicated; pool of all animals), together with distribution for 1000 shuffles of cell ordering (gray; p-values: one-tailed permutation tests). **e** For decoders trained with the activity of a single HD type (color-coded), cumulative histograms of MAE with matched or non-matched navigation modalities for training and testing data (p-values: two-tailed Kolmogorov–Smirnov tests). **f** Confidence (posterior probability) distribution across sessions for decoders in (**e**), indicating higher confidence in matched modalities, except for HD_I cells (p-values: two-tailed Wilcoxon tests). These results show that only pairs of HD_I cells maintain consistent temporal correlations across navigation modalities. Source data are provided as a Source Data file.

We also analyzed the normalized Frobenius distance between cell-pair correlation matrices corresponding to free vs. assisted sessions for each HD type, in order to quantify changes in the structure of temporal correlation across conditions. To quantify it, we used the mean of the squared difference between corresponding matrix elements, akin to the Frobenius distance (Fig. 2d). For HD_F and HD_A, the distance was comparable to that of the shuffled distribution, where cells were randomly sorted to construct each matrix. This suggests that the correlated activity between cell-pairs is primarily driven by either random or global fluctuations. In contrast, for HD_I cells, the distance was significantly smaller than that of the shuffled distribution. These results point to the lack of attractor dynamic behavior specifically in HD_F and HD_A cells.

To address population activity through a different perspective, we decoded head direction from the activity of each HD population using a Bayesian decoder within a cross-validation framework (Fig. 2e, f). The decoder performed significantly better for HD_F and HD_A cells when trained and tested with data from matched modalities, consistent with our previous results and with their definitions, but equally well across modalities for HD_I cells (Fig. 2e, f). Crucially, the confidence of the decoder, indicative of similar population activity patterns in training vs. testing data, followed similar trends, suggesting a reconfiguration of the population activity across sessions for HD_F and HD_A, but not HD_I cells (Fig. 2f).

These results rule out the possibility that the reconfiguration of directional codes across modalities is due to a lack of anchoring to external cues, suggesting instead profound changes in population activity patterns due to behavioral constraints.

https://doi.org/10.1038/s41467-026-70289-3



Assisted-navigation representations are sensory-focused

Since HD representatations are thought to rely on external sensory cues[2,18,20] or internal proprioception signals[34,35], we next asked if the activity of HD_A cells is modulated by changes in these input sources. We first repeated the previous experiment (cue-rich) but this time using an environment deprived of most external sensory cues (cue-poor; Fig. 3a; 1808 cells from 11 experimental days in 4 mice). In contrast with our previous findings, mean directional selectivity and stability in the cue-poor environment were not higher in assisted than in free sessions (Fig. 3b and Supplementary Fig. 7a, b). Similarly, the proportion of cells classified as HD was not significantly different from the proportion observed during free exploration (Fig. 3c). Crucially, MVL, stability, HD information and the proportion of cells classified as HD were higher during assisted navigation for the cue-rich than for the cue-poor environment, highlighting the role played by sensory cues in the reconfiguration of directional codes (Fig. 3b). These differences between representations of cue-rich and cue-poor contexts were not due to prior experience, as similar results were observed when

Fig. 3 | Assisted HD representations are sensory-focused. a Schematic of sensory cues in the default, cue-rich (left) and the cue-poor (right) environments. **b** Distribution across the pool of all recorded cells of the average MVL, HD information and stability (mean ± s.e.m.; two-tailed Mann–Whitney test for the comparison between cue-rich and cue-poor: p-values indicated for assisted sessions, $p > 0.14$ in all cases for free1 sessions except $p = 0.003$ for stability; Kruskal-Wallis tests across modalities in the cue-poor environment, $p < 0.0001$ in all cases). **c** Distribution across sessions of the fraction of cells classified as HD (mean ± s.e.m.; two-tailed Mann–Whitney test between cue-rich and cue-poor: $p = 0.002$ for assisted sessions and $p = 0.5$ for free1 sessions; two-tailed Friedman test across modalities in the cue-poor environment, $p = 0.4$). **d** Distribution across sessions of mean decoded error as in Fig. 1k for free and assisted sessions in cue-rich and cue-poor environments (color-coded; p-values: two-tailed Kolmogorov–Smirnov tests). **e** Representative examples (one cell per row; HD types indicated) of HD rate maps (black) and directional behavior (gray) across sessions of the speed-profile experiment, indicating MVL and peak event rate in Hz (P). Gray area: MVL above classification criterion. **f** Distribution across sessions of MVL, HD information, stability and fraction of cells classified as HD (6,357 cells from 7 mice in 17 sessions; p-values: Kruskal-Wallis test across assisted sessions for MVL, HD information and stability, two-tailed Friedman test across assisted sessions for the fraction of HD cells). **g** Each subpanel shows the directional maps of all cells (color code; one cell per row) belonging to a given HD type in a given speed-profile session (indicated). Red frame: session used to sort cells according to peak activity. **h** Distribution across cells of the mean Pearson correlation between HD maps for different sessions (indicated; mean ± s.e.m.; p-values: within HD type Kruskal-Wallis tests across assisted sessions). These results suggest that assisted navigation representations are closely linked to sensory cues rather than kinematic information. Source data are provided as a Source Data file.

including only animals that were first exposed to the assisted navigation in each context (Supplementary Fig. 7c, d). In line with this argument, a decoder trained with all recorded cells improved its performance during assisted navigation in the cue-rich but not the cue-poor environment (Fig. 3d). Such differences between cue-poor and cue-rich environments were much smaller, often not significant, during free foraging sessions (Fig. 3b).

We also asked if car speed modulated assisted directional representations in the cue-rich environment. We recorded activity during 4 consecutive sessions, each with a different speed regime, either random as in Fig. 1 or with an average speed set to the 30th (low), 50th (medium) or 70th (high) percentile of the free foraging speed distribution (Supplementary Fig. 7e, f; 6357 cells from 7 mice in 17 experimental days). We found no difference in mean directional selectivity, stability or proportion of cells classified as HD across speed sessions (Fig. 3e, f), which also applied to HD_A and HD_I considered separately (Supplementary Fig. 7 g). Furthermore, HD_A cells had strikingly consistent maps across speed regimes, with levels of directional correlation across assisted sessions similar to those of HD_I cells (Fig. 3e–h).

Put together, these results indicate that during assisted navigation, the directional code is strongly modulated by sensory cues.

Experience shapes assisted-navigation representations

Our results suggest a reversible dynamic in which HD_A replace HD_F cells for directional coding during assisted navigation. We next asked whether this new representation of a familiar environment is established instantaneously or gradually stabilized through learning. We divided the assisted session into five consecutive blocks (approximately 2 min each) and obtained HD maps for each block (Fig. 4a). We pooled data from cue-rich and speed experiments, all recorded in the cue-rich context, and divided them into two groups: sessions where assisted navigation was experienced for the first time by the mouse (naïve, 2233 cells from 7 mice in 7 experimental days) and sessions where it had prior exposure (trained, 3393 cells from 6 mice in 11 experimental days).

Using the Pearson correlation, and including all recorded cells, we first inspected the similarity between the HD maps for each block of the assisted session and the map corresponding to its last block. In naïve animals, but not in trained ones, we observed a significant increase in correlation across blocks, indicating an evolving representation (Fig. 4b and Supplementary Fig. 8a–c). In contrast, no significant trends were found when correlating maps for each block vs. maps for the previous free session (Supplementary Fig. 8d). This observation suggests that, while assisted-navigation representations evolve along the naïve session, they are already independent of free representations as early as block 1. Average MVL also increased with time spent in the task during naïve sessions, but remained unchanged during trained sessions. When analyzing individual HD types, a significant improvement in directional map quality was observed exclusively for HD_A cells during naïve sessions, but not during trained sessions or for HD_I cells (Supplementary Fig. 8c). Although there were no naïve free-exploration sessions available for comparison, we also assessed these variables for HD_F cells and found no significant changes across blocks (Supplementary Fig. 8f).

To understand these phenomena indicative of plasticity from the perspective of population coding, we decoded HD from population activity in each block, using the 4 remaining blocks as training data. We found that decoding error decreased as a function of time in the naïve session but not in subsequent ones (Fig. 4c and Supplementary Fig. 8e). Free exploration sessions did not exhibit a decrease in decoding error across blocks (Supplementary Fig. 8g).

These results suggest that plastic changes, occurring within minutes, shape assisted-navigation representations of direction into a new stable equilibrium. This newly established directional code is stored and remains readily accessible for use in subsequent experiences with assisted navigation.

Conjunctive codes for direction and space

Directional information, in some but not all brain areas where it is represented, is coded in conjunction with spatial information[2,36–38]. In conexts where correlations between behavioral variables such as position and direction are possible, the concept of unbiased information[36] allows for disentangling the contribution of each variable by quantifying the amount of information that cannot be explained by the other. Adapting this to our data[36], we asked if HD_A cells represent space along with direction. For each cell, we generated a series of new calcium event trains using a binomial random generator. Each instance was obtained based solely on the cell's original HD map and the animal's current heading at each timestamp, but not its position or spatial map. We refer to it as a HD-locked shuffled instance of the cell's event train, constructed to roughly preserve HD modulation and number of events. Unbiased spatial information was defined as the difference between the spatial information of the original map and the mean of the ones obtained for HD-locked shuffled instances (Fig. 5a). Conversely, we also produced spatially-locked shuffled instances and used them to define unbiased HD information. We found significant levels of unbiased spatial information for the pool of all recorded cells, as well as for all HD types considered separately (Fig. 5b and Supplementary Figs. 9-10a). In addition, we observed a positive correlation between unbiased spatial and directional information for HD_A cells, pointing to a conjunction of these codes during assisted navigation (Fig. 5b). This phenomenon could not be attributed to the conjunctive coding of HD by grid cells. As expected from previous studies[25,26], grid cells lost their spatial fields and exhibited low levels of unbiased spatial information during assisted sessions (Supplementary Fig. 11). These results point to entorhinal HD cells, and in particular HD_A, as bearing a conjuntive code.

We next asked if spatial associations in HD_A cells, as directional ones, were learned. We observed that unbiased spatial and directional information increased from the first to the second half of the assisted

https://doi.org/10.1038/s41467-026-70289-3

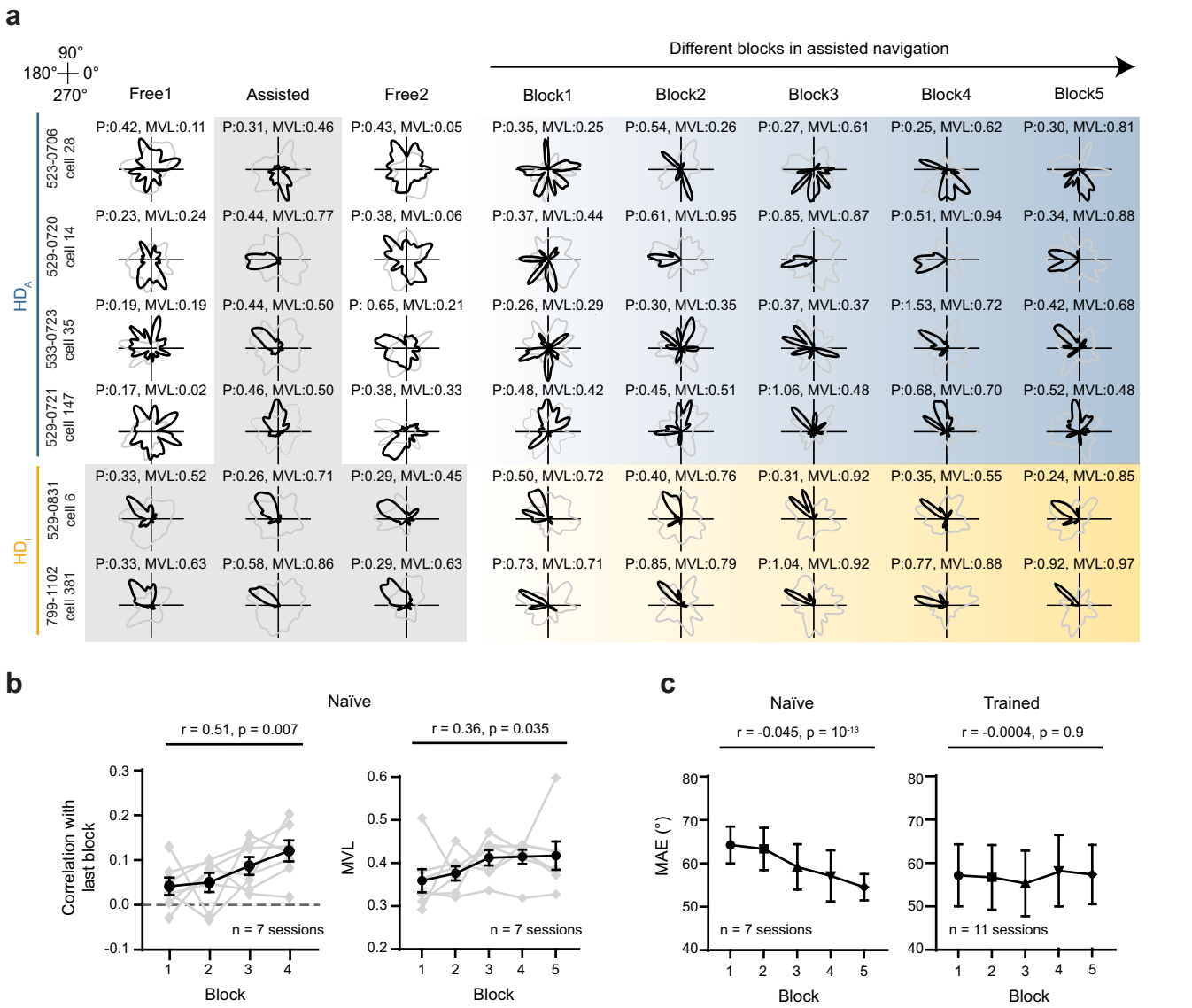


Fig. 4 | Progressive stabilization of assisted-navigation representations. **a** Representative examples of directional maps (black) and behavior distribution (gray) for HD_A and HD_I cells (one cell per row) across sessions (left) and across consecutive 2 min blocks of the assisted session (right). Peak event rate (P) and MVL indicated. **b** Distribution across sessions (mean: black; individual mice: gray) of the directional correlation between each block and the last block (left) and MVL (right) across blocks for all naïve sessions (mean ± s.e.m.; two-tailed Pearson correlation of each variable with time and p-values indicated). **c** Distribution across sessions of decoding error for naïve (left) and trained (right) sessions (mean ± s.e.m.; two-tailed Pearson correlation of each variable with time and p-values indicated). An improvement in decoded error was observed only for the naïve group. These results show that assisted-navigation directional codes are progressively learned, with increasing stabilization and refinement over time. Source data are provided as a Source Data file.

session during naïve but not trained sessions, for the pool of all recorded cells (Fig. 5c) and for HD_A cells in particular (Supplementary Fig. 10f). In agreement with these findings, the decoding of spatial information improved along the assisted session for naïve but not trained animals (Fig. 5d).

We also asked if conjunctive coding was favored by the presence of sensory cues along the walls of the arena during assisted navigation. We observed that spatial fields of HD cells tended to peak close to the walls, and significantly more during cue-rich than cue-poor sessions (Fig. 5e). We next asked if the preferred direction of firing could also be influenced by the closest wall. To address this, we defined theta as the angle between a cell's preferred direction and the direction from the center of its spatial field pointing toward the nearest wall (Fig. 5f). We found that the preferred direction of cells was significantly more skewed toward the closest wall in the cue-rich compared to the cue-poor environment (Fig. 5g). This wall-orientated preference, which could not be attributed to border-cell-like behavior (Supplementary Fig. 10a–e), was modulated by the distance between the field center and the wall: it was significant only in the cue-rich condition and for fields located within approximately 15 cm of the nearest wall. As fields farther away from the wall were included, the distribution of preferred directions became uniform. In contrast, in the cue-poor environment, preferred directions were uniformly distributed regardless of the distance to the nearest wall.

Our findings challenge the prevailing view that entorhinal HD cells represent a fixed cell class across behavioral conditions—a distinction that only becomes evident, however, through the partial reconfiguration of representations observed during assisted navigation. We show, instead, that cells can acquire a HD identity depending on the modality of navigation. While the population activity patterns of HD_F and HD_A cells are rapidly modified upon the first assisted experience, this reconfiguration involves cumulative, minute-by-minute changes that

https://doi.org/10.1038/s41467-026-70289-3

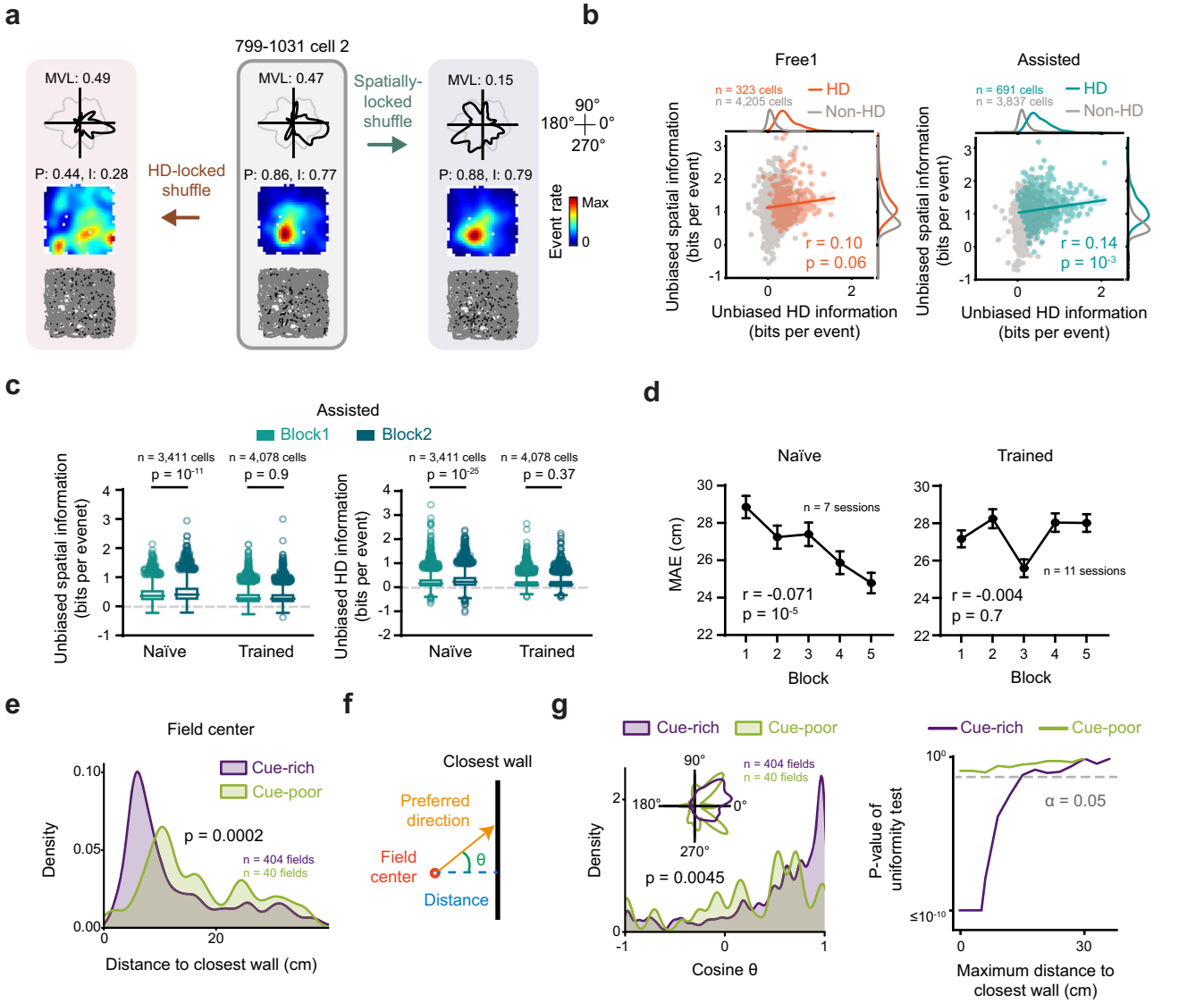


Fig. 5 | Concurrent learning of directional and spatial information during assisted navigation. a A representative example of HD-locked and spatially-locked shuffling (indicated; original maps in center column) used to assess unbiased information content. Each subpanel shows a directional map (top; behavioral map in gray and rate map in black), a spatial rate map (middle; color-coded; I: spatial information; P: peak event rate) and an event map (bottom; trajectory in gray and events in black dots). **b** Distribution of unbiased spatial and directional information across all cells, for free (left) and assisted (right) sessions. Color: cells classified as HD; gray: other cells; line: linear fit (mean ± s.e.m.; two-tailed Pearson correlation for HD cells, linear regression r and p-values indicated). **c** After dividing each assisted session into two consecutive equal blocks, distribution across cells of unbiased spatial and directional information for all cells recorded during naïve and trained sessions (indicated; p-values: two-tailed Wilcoxon tests). **d** Distribution across sessions of the error for decoding position along five consecutive blocks of naïve (left) and trained (right) assisted session (mean ± s.e.m.; two-tailed Pearson correlation r and p-values indicated). **e** Distribution of the distance from spatial field centers to the closest wall for cue-rich and cue-poor (color-coded) experiments (p-value: two-tailed Kolmogorov–Smirnov test). **f** Scheme showing theta as the angle between the cell's peak HD and the direction facing the wall closest to the spatial field center. **g** Left: Distribution of the cosine of theta (inset: distribution of theta), showing a stronger tendency in cue-rich relative to cue-poor environments to fire facing the closest wall (cosine close to 1; p-value: two-tailed Kolmogorov–Smirnov test). Right: p-value for a uniformity test pooling all fields with a maximum distance D to the closest wall vs. the distance D. These results suggest that HD and spatial information are acquired progressively, through a process that is modulated by the availability and proximity of sensory cues. Source data are provided as a Source Data file.

affect both the directional and spatial tuning of HD cells. As mice familiarize themselves with the new mode of navigation, these patterns gradually stabilize, bringing entorhinal directional maps to a new equilibrium. Importantly, this new equilibrium does not replace previously acquired representations of the environment but is added to a repertoire, remaining available for future use.

Discussion

Our main finding is that a substantial subset of entorhinal neurons can dynamically switch their functional role as head-direction (HD) cells in a familiar environment depending on the mode of navigation. Notably, other HD cells remain unaffected, arguing against the idea of impairment or complete remapping, suggesting instead an adaptation to behavioral constraints. Had we only observed a loss of function in HD cells, alternative explanations such as reduced attention could reasonably be hypothesized. However, the emergence of a stable new function—modulated by the availability of sensory cues—along with the overall increase in MVL and stability, is incompatible with such explanations. The functional role switch may result from the altered balance of sensory, motor, and vestibular inputs during assisted

navigation, leading to new equilibria in the integration and coding of sensory and self-motion information[39–42]. The stability and reversibility of this switch, with the original HD representation restored when free navigation resumes, indicate that the entorhinal cortex has the capacity to store and select from multiple maps for the same environment based on the mode of navigation. The adaptability we observe points to a self-organizing process, for example aimed at harmonizing observations and predictions[43], where the brain explores different solutions to maintain spatial and directional representations aligned with behavioral constraints. Together, these observations add to a growing body of evidence highlighting the flexibility of spatial and temporal representations in the entorhinal cortex[9,10,44–46].

Different forms of navigation have been shown to modulate place cell responses in the hippocampus[47–49]. In the entorhinal cortex, studies of passive transport—a manipulation akin to assisted navigation but lacking head fixation—have reported an impairment in the coding of navigational variables by certain functional types, such as grid cells, while generally preserving the directional representation by HD cells[25,26]. In contrast, our manipulations result in approximately half of the HD cells recorded during free foraging sessions losing their tuning under assisted navigation. This discrepancy may stem from differences across species, as previous studies involved rats and ours utilizes mice. Additionally, a key feature in our manipulation is the head-fixed exploration of the open field during assisted navigation, which may disrupt feedback loops involving the vestibular and motor systems[50]. Numerous studies highlight differences in spatial coding between freely moving and fully head-fixed animals navigating virtual environments[39,40,42]. Evidence suggests that purely angular coordination between motor and vestibular inputs, with no forward coordination, is enough to maintain entorhinal HD coding intact in such setups[41]. A major distinction of our approach is that animals physically move in the environment while their head is fixed to the autonomous driving cart, providing more realistic vestibular and sensory feedback. Regardless of the technical factors that explain the discrepancies with previous results, the key insight of our findings lies in the emergence of a new population of HD cells during assisted navigation, compensating for the group that loses directional tuning.

Our results suggest that HD is encoded in the entorhinal cortex under two distinct regimes. On one hand, HD_I cells exhibit an invariant directional representation that remains stable across different navigation modalities, consistent with attractor dynamics[35,51–53]. On the other hand, HD_F and HD_A cells are navigation-mode specific, with HD_A cells showing a strong modulation by sensory enrichment. A somewhat similar distinction has been noted before between entorhinal HD cells affected vs. unaffected by contextual changes, although in that study contextual variability alone did not induce functional-role switches[20]. Similarly, a report of spontaneous remapping during virtual navigation has highlighted the entorhinal cortex's capacity to store multiple spatial representations of a given virtual context[42]. However, in that case, remapping was not clearly linked to behavioral constraints, and neither functional type switches nor head direction coding were explicitly addressed, likely due to limitations inherent to navigation in one-dimensional virtual environments[40,41]. Our study, therefore, introduces the concept of an entorhinal HD code in which a fixed template coexists with a more flexible representation shaped by the dynamic ways in which animals interact with their environment.

HD cells across various brain regions are known to conjunctively encode spatial information, either in periodic patterns[2] or more irregular, dispersed forms[36]. This mixture is also observed in the hippocampus, where place cells are modulated by goal locations or reference points[37,38,54], and perhaps in the spatial-view responses observed in primates[55]. Leveraging the creation of new representations in a familiar environment during assisted navigation, our findings demonstrate that learning plays a crucial role in shaping the spatial tuning curves of entorhinal HD cells. Specifically, we found that HD_A cells develop spatio-directional fields tuned to the walls of sensory-enriched environments, but show diminished tuning in sensory-deprived environments, highlighting the role of plasticity in associating cell activity with the salience of sensory cues.

Entorhinal representations are traditionally thought to arise from either hard-wired mechanisms or principles of self-organization. Recent evidence, for instance, suggests that substantial components of entorhinal[56] or anterior-dorsal thalamic[57] attractor dynamics are present before animals accumulate significant experience with the world, highlighting the critical role of processes that function as if they were innate or hard-wired during early development. Our findings, however, offer evidence of a complementary dynamic: the remarkable flexibility of entorhinal cells to adapt through learning, reshaping their functional identity in response to a shifting balance between sensory and self-motion inputs. Although we cannot exclude the possibility that these changes originate upstream, a self-organizing process provides the most parsimonious explanation, given the observation that cells improve their tuning during their first experience in assisted navigation. Together, hard-wired templates and self-organizing mechanisms may serve as complementary driving forces in entorhinal processing, providing a flexible framework capable of meeting the challenges posed by multimodal inputs and diverse forms of interaction with the external world.

Methods

Animals

All experimental procedures were approved by the Institutional Animal Care & Use Committee at Peking University. Adult male C57BL/6 N mice ($n = 12$) were used for experiments, housed under 20 °C, 50% humidity in a 12 h light/dark cycle individually. Male mice were used because they exhibited more consistent running behavior in the openfield. Their total food intake (2–4 g of food per day) was controlled and monitored to maintain 90% of free-feeding body weight. Behavioral experiments were performed during the dark phase. All data for all mice were included for analysis.

Virus injection and prism implantation

All surgeries were performed on isoflurane (airflow: 0.8–1.0 L/min, 0.5–3% isoflurane, adjusted according to physiological condition) anaesthetized animals head fixed on a stereotaxic frame (KOPF). The hair was trimmed from the head, followed by the cleaning of the incision area with alcohol and betadine. After cleaning tissues and blood on the skull, a small square craniotomy was made with a thin drill over the right MEC. The dura was then removed by a blunt needle to expose the brain surface. For each mouse, two injections of total 0.8 µL of AAV-hSyn-GCaMP6f (titer: $>2 \times 10^{13}$ vg/mL) were injected into the right MEC at a rate of 30 nL/min with a glass micropipette (typical two injection sites: +3.1 to +3.7 mm ML, sinus + 0.3 mm AP, −1.8 to −1.4 mm and −1.5 to −1.3 mm DV), controlled by a Nanoliter 2020 Microinjection Pump (World Precision Instruments). The pipette was left in place for 10 min before being slowly withdrawn to allow virus diffusion. Next, a $3.5 \times 2.5\ mm^2$ prism (Grintech) was inserted between cerebellum and cerebrum with the flat surface targeted on dorsoventral surface of MEC. Craniotomy was then covered with Kwik-Sil (World Precision Instruments) and tissue adhesive glue (3 M) to protect and bond the skull with the scalp incision area. A headbar (Transcend Vivoscope) was added on the top, with the exposed skull as well as the gaps between the skull and the headbar filled with dental cement (Super bond). Animals were then placed on a heating pad until waking up and housed individually while being treated with cephalosporin for 1 week.

Miniaturized 2-photon microscope calcium imaging

Mice were allowed to recover for three weeks after surgery and then restrained with an adapter. Using a wide-field single-photon microscope, a field of view (FOV) was determined in which the largest

number of neurons appeared clearly, and a baseplate was then attached to the headbar to fix the microscope. During calcium imaging, the calcium signals were collected with the miniatured 2-photon microscope (LFMTPM V2.0.1), and controlled by the GINKGO-MTPM software (Transcend Vivoscope Biotech Co., Ltd, China). Two-photon excitation of GCaMP6 was achieved using a laser (TVS-FL-01, Transcend Vivoscope Biotech Co., Ltd China) at 920 nm with a typical laser intensity of 70 mW. Images were acquired at 9.5 Hz at a resolution of 600 × 512 pixels corresponding to a field of view of 534 × 455 µm. The imaging data was recorded synchronously with the behavioral data using the GINKGO-MTPM software. After recording, behavioral data were aligned with the imaging clock and downsampled to the imaging frame rate (9.5 Hz) by linear interpolation.

Some animals were re-used after a month, which explains the discrepancy between number of mice and experimental days in some of our results. In those cases, the baseplate was re-attached to the headbar to obtain a better FOV. The new imaged neurons were added to the statistics, considering the two sessions with different FOV as independent from each other. While this procedure could potentially result in some bias, Supplementary Fig. 3a, b shows that our main observations hold robustly if only one experimental day per mouse is taken into account.

Histology

After finishing experiments, mice were first anaesthetized with a 0.6 mL injection of 2.5% tribromoethanol and then fixed on the perfusion table. An incision was made along the midline of the abdomen to the chest with dissecting scissors, and a perfusion needle was inserted into the left ventricle once an incision was made on the right atrium. Mice were then transcardially perfused with 40 mL saline, followed by 20 mL 4% paraformaldehyde (PFA). After perfusion, the brain tissue was carefully removed, post-fixed in 4% PFA for more than 24 h at 4 °C, and then dehydrated in 30% sucrose until the brain sank. Next, the brain tissue was removed from the sucrose and mounted on a metal platform with OCT Compound (4583, Sakura, Tokyo, Japan). After freezing in the cryostat, the tissue was sectioned at a thickness of 30-µm.

Sections were first rinsed with PBS two times (300 µL each slide, 5 min each time), incubated with blocking solution (10% goat serum and 0.3% Triton X-100 in PBS) for 1 h at room temperature, followed by primary antibody (chicken anti-GFP, Invitrogen, Cat #A10262; rabbit anti-NeuN, Abcam, Cat #ab_177487) in diluted (1:1000) blocking solution overnight at 4 °C. After washing in PBS three times (300 µL each slide, 5 min each time), sections were then incubated with species-specific secondary antibodies (Alexa Fluor 488, Invitrogen, Cat #A11039; Alexa Fluor 568, Abcam, Cat #ab_175471) and DAPI (Sigma-Aldrich) in diluted (1:1000) blocking solution for 2–4 h at room temperature. After rinsing with PBS two times (300 µL each slide, 5 min each time), sections were mounted on glass slides with Fluoromount-G (SouthernBiotech) and coverslipped. Imaging was processed using either Zeiss Axio Scan Z1 or Olympus Virtual Slide System to confirm the position of prism implantation and the expression of virus.

Free exploration task

After complete recovery from the surgery, mice were habituated in a 40 cm high and 80 cm side square arena for more than 3 days (at least 15 min per day). The walls and the floor of the arena were built using plastic. In the cue-poor environment, three cue cards (30 cm W × 21 cm H) with different symbols were placed in the centers of three walls, with the bottom edge 8 cm above the floor. In the cue-rich environment, all walls were further covered with gratings and an extra odor cue (pure ethyl acetate diluted to 5% v/v in mineral oil) was placed in the center of the fourth wall. Neural activity was recorded as the animal freely explored in the arena, searching for butter cookies (PAUL KEI) that were thrown into the arena one at 10–15 s intervals. Mouse behavior was monitored at 25 frames per second (fps) with an infra-red camera centered above the arena. The arena was cleaned with dust collector and 75% ethanol between sessions.

Assisted navigation task

Mice were restrained head-fixed to a custom-made autonomous-driving car and moved around the same arena. The car had one motor (WHEELTE) on each side and was controlled by an Arduino board powered by six rechargeable batteries (Delipow, 2700 mA). The two motors operated in the same direction during forward movements and in opposite directions during turning. To manipulate the car moving at low speeds, motors with high reduction ratio were used. To mimic the random foraging of mice, the car was set to change its moving direction after an interval of time drawn from a uniform distribution between 100 and 1500 ms. Unless a wall was encountered, there was a 92.5% chance of proceeding forward, a 7% chance of turning left or right, and a 0.5% chance of stopping. Once the choice was made, the car would execute the action until the next decision point. During the forward mode, the ultrasound sensors in front of the car detected the distance from the wall every 100 ms. The car would move backwards and make a turn away from the wall if the distance was smaller than 5 cm. In the default, random speed regime, the moving speed of the car changed at every decision point. The new speed was obtained from a pseudo-random uniform distribution between 2 and 30 cm s^{-1}.

Speed modulation task

Speed modulation was implemented by changing the parameters of the Arduino code. The moving speed of mice during free exploration in previous experiments was collected, and its 30th, 50th, and 70th percentile were set to the car as a constant value for low, medium and high-speed conditions (see Supplementary Fig. 7e, f).

Pre-processing of 2-photon calcium signal

After recording, Ca^{2+} imaging data were first analyzed offline using Suite2P[58] (https://github.com/MouseLand/suite2p) for motion correction, identification, and extraction of spatial footprints as well as the activity traces of region of interest (ROI). The outputs from Suite2P were further analyzed with custom-written programs in Matlab (R2020a, The MathWorks, Natick, MA) for calculating Ca^{2+} signals for each specified ROI as the relative fluorescence changes ($\Delta F/F$)[59]. $\Delta F/F$ was then deconvolved using OASIS[60] (https:// github.com/zhoupc/OASIS_matlab). To extract calcium transients from noise such as electrical and motion artifacts, significant transients were identified as periods in which $\Delta F/F$ was two standard deviations above the baseline fluorescence for more than 0.75 s, as established in previous studies[61,62]. For each ROI, a fluorescence change was identified as a true calcium event only during significant transients when its amplitude exceeded one standard deviation above the baseline. To count the cells recorded in each animal, CellReg[63] (https://github.com/zivlab/CellReg) was applied to identify the same cells across days within each re-attachment.

Tracking of behavioral data

The raw behavioral data recorded by the camera was analyzed using DeepLabCut[64] (https://github.com/DeepLabCut/DeepLabCut). For each frame, four body parts (free exploration: nose, neck, left and right ear; assisted navigation: nose, neck, left and right side of the headbar) were extracted to yield the position of the animal. The DLC model was trained from 50 manually labeled datasets with resnet_50 for 100,000 iterations. The identified positions located inside the arena were kept and further smoothed with a 15-point mean filter. Head direction (HD) was determined by the relative position of the animal's neck and nose.

Spatial and directional rate maps

For each session, cells with more than 50 calcium events were extracted, and rate maps were generated to evaluate their calcium

activity normalized by occupancy (sessions where a cell had less then 50 calcium events were not included in the analyses). The deconvolved calcium activity was first sorted into different bins (bin size: 3×3 cm^2 for spatial maps and 3° for directional maps) according to the behavioral data, and then divided by the time spent in each bin. The resulting rate was further smoothed either using a 2D Gaussian kernel with a standard deviation of 6 cm for spatial maps or a 30° mean window filter for directional maps. For spatial rate maps, the firing fields were determined as the contiguous periods exceeding 60th percentile of the field's peak rate, with the peak rate higher than 0.5 Hz. All data with running speeds lower than 2 cm per second were excluded in all calculations to rule out the effects of different behavioral states.

Analysis of head direction cells

The length of mean resultant vector (mean vector length, MVL) was calculated for each cell to evaluate HD selectivity. MVL was obtained by averaging the vectors corresponding to each bin of the directional rate map using the circular statistic toolbox in Matlab[65]. Shuffling was performed 1000 times for each cell. For a single shuffling instance, a shuffled directional map was obtained by time-shifting the deconvolved calcium activity of the cell along the animal's path wrapping the end of the session to the beginning, with a 30 s exclusion window toward the future and the past. Shuffled MVL values were calculated and pooled for all cells in the first free foraging session to obtain the 99th percentile of the distribution, which was set as a criterion to classify cells as HD in all sessions. In all the experiments, cells that passed the criterion during the first free exploration session but not during the assisted session were classified as HD_F. Conversely, cells that passed the criterion only during assisted sessions but not during any of the free exploration sessions were identified as HD_A. Finally, cells that passed the criterion in both conditions were classified as HD_I.

HD information was used as a complementary measure of directionality, with the advantage of not being biased by the potential presence of multiple opposite directional fields[66]. It was calculated as

$$I = \sum_i p_i \lambda_i \log_2 \frac{\lambda_i}{\lambda}, \tag{1}$$

where λ_i is the mean event rate of a unit in the ith angular bin, λ is the average event rate of the neuron, and p_i is the probability of the animal's in the ith bin. Directional stability was calculated as the Pearson correlation of the directional maps obtained for the two consecutive halves of a session.

Analysis of spatial cells

Spatial information was calculated as HD information but using the spatial map and spatial bins. Shuffling was performed similarly, and a cell was identified as a spatial cell if its spatial information exceeded the 99th percentile of the spatial information for the pooled shuffled data. Spatial stability was calculated as the Pearson correlation of the spatial maps obtained for the two consecutive halves of a session.

Analysis of grid cells

Spatial autocorrelation was obtained for each cell as in previous studies[2] to identify grid cells. The autocorrelogram was calculated as the correlation between the fields with spatial lags of τ_x and τ_y as

$$r(\tau_x - \tau_y) = \frac{n\sum\lambda(x-y)\lambda(x-\tau_x, y-\tau_y) - \sum\lambda(x,y)\sum\lambda(x-\tau_x, y-\tau_y)}{\sqrt{n\sum\lambda(x,y)^2 - (\sum\lambda(x,y))^2}\sqrt{n\sum\lambda(x-\tau_x, y-\tau_y)^2 - (\sum\lambda(x-\tau_x, y-\tau_y))^2}} \tag{2}$$

Where $\lambda(x,y)$ is the average event rate of a neuron at location (x,y), and the summation is over all n pixels in $\lambda(x,y)$ for which the rate was calculated for both $\lambda(x,y)$ and $\lambda(x-\tau_x, y-\tau_y)$. Autocorrelations were not estimated where $n < 20$.

To quantify the 6-fold symmetry within the spatial autocorrelation map, a circular sample of the autocorrelogram was extracted, centered on the central peak but with the central peak excluded, and compared with its rotated version. The degree of spatial periodicity ('grid score') was obtained as the difference between the lowest correlation at 60° and 120° and the highest correlation at 30°, 90° and 150°. Shuffling was performed for each cell with 1000 permutations. For each cell, the control spatial map was obtained by time-shifting the deconvolved calcium activity of the cell along the animal's path by a random number of frames taken from a uniform distribution including the whole session, but excluding 30 s into the future or the past, to ensure the complete loss of correlation between neural activity and behavior. A cell was identified as a grid cell if its grid score from the experimental data exceeded the 99th percentile of pooled shuffled data.

Calculation of unbiased information

Unbiased information was used to remove the part of spatial information strictly due to directional responses and vice-versa[36,67,68]. For a given cell, a spatially-locked shuffled instance was defined by a new calcium event train generated through a binomial random process. For every timestamp, this random process had a mean given by the value of the spatial map in the bin where the animal stood. Similarly, a HD-locked shuffled instance used the HD map to generate a new event train. Spatial and HD information were calculated for each of the 100 shuffles of each type per cell. The unbiased spatial information for a cell was defined as the difference between its actual spatial information and the mean of the shuffled spatial information. The unbiased HD information was defined as the difference between its actual HD information and the mean of the shuffled HD information.

Similarly, and to allow a comparison of variables with the same methodology, the unbiased grid score, unbiased border score and unbiased spatial information were calculated as the difference between the observed variable and the average over 100 spatial shuffles for each cell.

Calculation of directionality

For a collection of spatial bins (typically those inside the center square vs close to the walls), the behavioral-MVL for each bin was obtained similarly to the MVL but using the distribution of head directions instead of the rate map. The directionality of each bin was defined as the average behavioral-MVL across sessions.

Downsampling of behavioral data

To rule out the possibility that the reconfiguration across conditions was caused by differences in the distribution of speed during free and assisted session, behavioral data in each condition was downsampled to achieve similar moving speeds. For each recording, the behavioral data during assisted navigation was first downsampled in speed bins where it occurred in excess, to match the speed distribution of free sessions on the same day. The behavioral data recorded in free exploration was then downsampled where it occurred in excess, to match exactly the speed distribution that resulted from the first round of downsampling. Spatial and directional rate maps were then obtained from downsampled data.

Calculation of best rotated angle

To evaluate whether a HD_I cell remapped across conditions, the best rotated angle was defined as the amount of rotation (in multiples of 3°) of the map corresponding to the first session required to maximize its Pearson correlation with the map corresponding to the second session.

Correlation between cell pairs

To study the structure of cell-pair activity correlations we first divided free and assisted sessions into two consecutive halves. To study HD_F and HD_I, the first half of the free session was used to sort cells according to their preferred direction. The correlation matrix was then calculated for each half of each session, where element (i,j) had the Pearson correlation between the corresponding event train of cells i and j. The presence of a diagonal in the correlation matrix, indicative of similar activity between similarly sorted cells, was evaluated for all sessions not used for sorting. HD_A cells were studied similarly but using the second half of the assisted session to sort cells. In-diagonal elements were defined as the 10% closest to the diagonal, but excluding it, while off-diagonal elements were defined as the 10% furthest apart from the diagonal. For each HD type, only sessions containing more than 10 cells of that type were included in the analysis.

Shuffling instances of the correlation matrix were obtained by randomly sorting the cells and calculating the correlation between corresponding cell pairs.

Decoding from neural data

A Naïve Bayes decoder with 5-fold cross validation was applied to decode the position and HD of the animal from neural activity[69]. Only sessions containing more than 5 cells were included. Each session was divided into 5 consecutive blocks.

First, the average firing rate in response to position can be measured by a tuning curve $f_i(X)$ for each cell i. We assumed the probability of the cell producing n events during a short time interval γ (set to 1 s in our analysis) for a fixed position X followed a Poisson statistic

$$P(n|X) = (f(X) \cdot \gamma)^n e^{-\gamma f(X)}/n!, \tag{3}$$

We further assumed the firing rate is independent across cells. According to Bayes' theorem, given the activity of neuron populations, the conditional distribution for position X could be represent as

$$P(X|n) = CP(X)\left(\prod_{i=1}^{N} f_i(X)^{n_i}\right) e^{-\gamma\sum_{i=1}^{N} f_i(X)}, \tag{4}$$

where X is the specified position bin, each cell i has a tuning curve $f_i(X)$, and fired n_i times during time window γ. P(X) is calculated as the overall probability of the animal staying in the spatial bin X. C is a normalization constant calculated so that the total probability is 1. For each frame, the decoded position was determined as the position with the maximum posterior probability (confidence). Shuffled data were generated by randomly time-shifting and wrapping the position of animals. The decoding accuracy was obtained by test data for each fold of cross-validation, calculated as the mean absolute error (MAE) between the observed and decoded positions. To decode HD, the same procedure was applied, with X indicating the directional bin.

Statistics and reproducibility

No statistical methods were used to predetermine sample sizes. Sample sizes were chosen based on previous publications and prior experience in our laboratory. The study contains data from 12 mice. All collected data were analyzed, with inclusion critferia for specific analyses described in Methods. Cells with fewer than 50 events were excluded. Sessions containing fewer than 5 or 10 recorded cells were excluded from decoding and temporal correlation analyses, respectively, to minimize noise and improve reliability.

Animals were randomly allocated into each experiment group. Experimenters were not blinded to group allocation during data collection. However, neural activity during behavioral tasks could only be observed after automatic pre-processing. Experimenters were blinded to experimental conditions during data analysis. Each animal in the study is an independent experimental replicate performed separately. Results were consistent across animals.

Data analysis were conducted using MATLAB (R2022a), Python (3.8) and GraphPad Prism 9. Figures were generated using MATLAB, Python and GraphPad Prism 9 and arranged in Adobe Illustrator 2023. Statistical analyses were performed using MATLAB, Python and GraphPad Prism 9.

Reporting summary

Further information on research design is available in the Nature Portfolio Reporting Summary linked to this article.

Data availability

Data included in this study are available on Figshare (https://doi.org/10.6084/m9.figshare.30344758). Source data are provided with this paper.

Code availability

Custom code supporting this work is available at GitHub (https://github.com/RuojinLiu/assisted_movement).

References

1. Fyhn, M., Molden, S., Witter, M. P., Moser, E. I. & Moser, M. B. Spatial representation in the entorhinal cortex. *Science* **305**, 1258–1264 (2004).
2. Sargolini, F. et al. Conjunctive representation of position, direction, and velocity in entorhinal cortex. *Science* **312**, 758–762 (2006).
3. Munn, R. G. & Giocomo, L. M. Multiple head direction signals within entorhinal cortex: origin and function. *Curr. Opin. Neurobiol.* **64**, 32–40 (2020).
4. Moser, E. I., Kropff, E. & Moser, M. B. Place cells, grid cells, and the brain's spatial representation system. *Annu. Rev. Neurosci.* **31**, 69–89 (2008).
5. Sun, C. et al. Distinct speed dependence of entorhinal island and ocean cells, including respective grid cells. *Proc. Natl. Acad. Sci. USA* **112**, 9466–9471 (2015).
6. Rowland, D. C. et al. Functional properties of stellate cells in medial entorhinal cortex layer II. *Elife* **7**, e36664 (2018).
7. Tukker, J. J. et al. Microcircuits for spatial coding in the medial entorhinal cortex. *Physiol. Rev.* **102**, 653–688 (2022).
8. Barry, C., Hayman, R., Burgess, N. & Jeffery, K. J. Experience-dependent rescaling of entorhinal grids. *Nat. Neurosci.* **10**, 682–684 (2007).
9. Boccara, C. N., Nardin, M., Stella, F., O'Neill, J. & Csicsvari, J. The entorhinal cognitive map is attracted to goals. *Science* **363**, 1443–1447 (2019).
10. Butler, W. N., Hardcastle, K. & Giocomo, L. M. Remembered reward locations restructure entorhinal spatial maps. *Science* **363**, 1447–1452 (2019).
11. Krupic, J., Bauza, M., Burton, S., Barry, C. & O'Keefe, J. Grid cell symmetry is shaped by environmental geometry. *Nature* **518**, 232–235 (2015).
12. Krupic, J., Bauza, M., Burton, S. & O'Keefe, J. Local transformations of the hippocampal cognitive map. *Science* **359**, 1143–1146 (2018).
13. Malone, T. J. et al. A consistent map in the medial entorhinal cortex supports spatial memory. *Nat. Commun.* **15**, 1457 (2024).
14. Yoon, K. et al. Specific evidence of low-dimensional continuous attractor dynamics in grid cells. *Nat. Neurosci.* **16**, 1077–1084 (2013).
15. Clark, B. J., Brown, J. E. & Taube, J. S. Head direction cell activity in the anterodorsal thalamus requires intact supragenual nuclei. *J. Neurophysiol.* **108**, 2767–2784 (2012).
16. Peyrache, A., Lacroix, M. M., Petersen, P. C. & Buzsáki, G. Internally organized mechanisms of the head direction sense. *Nat. Neurosci.* **18**, 569–575 (2015).

17. Winter, S. S., Clark, B. J. & Taube, J. S. Disruption of the head direction cell network impairs the parahippocampal grid cell signal. *Science* **347**, 870–874 (2015).
18. Jacob, P. Y. et al. An independent, landmark-dominated head-direction signal in dysgranular retrosplenial cortex. *Nat. Neurosci.* **20**, 173–175 (2017).
19. Dudchenko, P. A., Wood, E. R. & Smith, A. A new perspective on the head direction cell system and spatial behavior. *Neurosci. Biobehav. Rev.* **105**, 24–33 (2019).
20. Kornienko, O., Latuske, P., Bassler, M., Kohler, L. & Allen, K. Non-rhythmic head-direction cells in the parahippocampal region are not constrained by attractor network dynamics. *Elife* **7**, e35949 (2018).
21. Taube, J. S. Head direction cells recorded in the anterior thalamic nuclei of freely moving rats. *J. Neurosci.* **15**, 70–86 (1995).
22. Stackman, R. W., Golob, E. J., Bassett, J. P. & Taube, J. S. Passive transport disrupts directional path integration by rat head direction cells. *J. Neurophysiol.* **90**, 2862–2874 (2003).
23. Shinder, M. E. & Taube, J. S. Active and passive movement are encoded equally by head direction cells in the anterodorsal thalamus. *J. Neurophysiol.* **106**, 788–800 (2011).
24. Shinder, M. E. & Taube, J. S. Self-motion improves head direction cell tuning. *J. Neurophysiol.* **111**, 2479–2492 (2014).
25. Winter, S. S., Mehlman, M. L., Clark, B. J. & Taube, J. S. Passive transport disrupts grid signals in the parahippocampal cortex. *Curr. Biol.* **25**, 2493–2502 (2015).
26. Kropff, E., Carmichael, J. E., Moser, E. I. & Moser, M. B. Frequency of theta rhythm is controlled by acceleration, but not speed, in running rats. *Neuron* **109**, 1029–1039 (2021).
27. Zong, W. J. et al. Fast high-resolution miniature two-photon microscopy for brain imaging in freely behaving mice. *Nat. Methods* **14**, 713–719 (2017).
28. Taube, J. S. The head direction signal: origins and sensory-motor integration. *Annu Rev. Neurosci.* **30**, 181–207 (2007).
29. Skaggs, W. E., Knierim, J. J., Kudrimoti, H. S. & McNaughton, B. L. A model of the neural basis of the rat's sense of direction. *Adv. Neural Inf. Process Syst.* **7**, 173–180 (1995).
30. Zhang, K. Representation of spatial orientation by the intrinsic dynamics of the head-direction cell ensemble: a theory. *J. Neurosci.* **16**, 2112–2126 (1996).
31. Kim, S. S., Rouault, H., Druckmann, S. & Jayaraman, V. Ring attractor dynamics in the central brain. *Science* **356**, 849–U111 (2017).
32. Gardner, R. J., Lu, L., Wernle, T., Moser, M. B. & Moser, E. I. Correlation structure of grid cells is preserved during sleep. *Nat. Neurosci.* **22**, 598 (2019).
33. Gardner, R. J. et al. Toroidal topology of population activity in grid cells. *Nature* **602**, 123 (2022).
34. Valerio, S. & Taube, J. S. Path integration: how the head direction signal maintains and corrects spatial orientation. *Nat. Neurosci.* **15**, 1445–1453 (2012).
35. Spalla, D., Treves, A. & Boccara, C. N. Angular and linear speed cells in the parahippocampal circuits. *Nat. Commun.* **13**, 1907 (2022).
36. Peyrache, A., Schieferstein, N. & Buzsáki, G. Transformation of the head-direction signal into a spatial code. *Nat. Commun.* **8**, 1752 (2017).
37. Sarel, A., Finkelstein, A., Las, L. & Ulanovsky, N. Vectorial representation of spatial goals in the hippocampus of bats. *Science* **355**, 176–180 (2017).
38. Jercog, P. E. et al. Heading direction with respect to a reference point modulates place-cell activity. *Nat. Commun.* **10**, 2333 (2019).
39. Aghajan, Z. M. et al. Impaired spatial selectivity and intact phase precession in two-dimensional virtual reality. *Nat. Neurosci.* **18**, 121–128 (2015).
40. Minderer, M., Harvey, C. D., Donato, F. & Moser, E. I. Virtual reality explored. *Nature* **533**, 324–325 (2016).
41. Chen, G., King, J. A., Lu, Y., Cacucci, F. & Burgess, N. Spatial cell firing during virtual navigation of open arenas by head-restrained mice. *Elife* **7**, e34789 (2018).
42. Low, I. I. C., Williams, A. H., Campbell, M. G., Linderman, S. W. & Giocomo, L. M. Dynamic and reversible remapping of network representations in an unchanging environment. *Neuron* **109**, 2967–2980.e2911 (2021).
43. Campbell, M. G. et al. Principles governing the integration of landmark and self-motion cues in entorhinal cortical codes for navigation. *Nat. Neurosci.* **21**, 1096–1106 (2018).
44. Bowler, J. C., Azhar, D., Jensen, C. M., Lee, H. W. & Heys, J. G. Structured experience shapes strategy learning and neural dynamics in the medial entorhinal cortex. Preprint at https://doi.org/10.1101/2025.05.13.653873 (2025).
45. Wen, J. H., Sorscher, B., Aery Jones, E. A., Ganguli, S. & Giocomo, L. M. One-shot entorhinal maps enable flexible navigation in novel environments. *Nature* **635**, 943–950 (2024).
46. Bigus, E. R., Lee, H. W., Bowler, J. C., Shi, J. & Heys, J. G. Medial entorhinal cortex mediates learning of context-dependent interval timing behavior. *Nat. Neurosci.* **27**, 1587–1598 (2024).
47. Terrazas, A. et al. Self-motion and the hippocampal spatial metric. *J. Neurosci.* **25**, 8085–8096 (2005).
48. Green, L., Tingley, D., Rinzel, J. & Buzsaki, G. Action-driven remapping of hippocampal neuronal populations in jumping rats. *Proc. Natl. Acad. Sci. USA* **119**, e2122141119 (2022).
49. Geva-Sagiv, M., Romani, S., Las, L. & Ulanovsky, N. Hippocampal global remapping for different sensory modalities in flying bats. *Nat. Neurosci.* **19**, 952–958 (2016).
50. Meyer, A. F., O'Keefe, J. & Poort, J. Two distinct types of eye-head coupling in freely moving mice. *Curr. Biol.* **30**, 2116–2130.e2116 (2020).
51. Knierim, J. J. & Zhang, K. Attractor dynamics of spatially correlated neural activity in the limbic system. *Annu. Rev. Neurosci.* **35**, 267–285 (2012).
52. Khona, M. & Fiete, I. R. Attractor and integrator networks in the brain. *Nat. Rev. Neurosci.* **23**, 744–766 (2022).
53. Chaudhuri, R., Gercek, B., Pandey, B., Peyrache, A. & Fiete, I. The intrinsic attractor manifold and population dynamics of a canonical cognitive circuit across waking and sleep. *Nat. Neurosci.* **22**, 1512–1520 (2019).
54. Acharya, L., Aghajan, Z. M., Vuong, C., Moore, J. J. & Mehta, M. R. Causal Influence of visual cues on hippocampal directional selectivity. *Cell* **164**, 197–207 (2016).
55. Rolls, E. T. Hippocampal spatial view cells for memory and navigation, and their underlying connectivity in humans. *Hippocampus* **33**, 533–572 (2023).
56. Guardamagna, M. et al. Experience-independent emergence of toroidal and ring manifolds in the entorhinal cortex. in *Society for neuroscience*. **17**, (Chicago, 2024).
57. Bassett, J. P., Wills, T. J. & Cacucci, F. Self-organized attractor dynamics in the developing head direction circuit. *Curr. Biol.* **28**, 609–615.e603 (2018).
58. Pachitariu, M. et al. Suite2p: beyond 10,000 neurons with standard two-photon microscopy. Preprint at https://doi.org/10.1101/061507 (2017).
59. Zong, W. J. et al. Large-scale two-photon calcium imaging in freely moving mice. *Cell* **185**, 1240 (2022).
60. Friedrich, J., Zhou, P. & Paninski, L. Fast online deconvolution of calcium imaging data. *Plos Comput. Biol.* **13**, e1005423 (2017).
61. Low, R. J., Gu, Y. & Tank, D. W. Cellular resolution optical access to brain regions in fissures: imaging medial prefrontal cortex and grid cells in entorhinal cortex. *Proc. Natl. Acad. Sci. USA* **111**, 18739–18744 (2014).
62. Zong, W. et al. Large-scale two-photon calcium imaging in freely moving mice. *Cell* **185**, 1240–1256.e1230 (2022).

63. Sheintuch, L. et al. Tracking the same neurons across multiple days in Ca(2+) Imaging Data. *Cell Rep.* **21**, 1102–1115 (2017).
64. Nath, T. et al. Using DeepLabCut for 3D markerless pose estimation across species and behaviors. *Nat. Protoc.* **14**, 2152–2176 (2019).
65. Berens, P. CircStat: a MATLAB toolbox for circular statistics. *J. Stat. Softw.* **31**, 1–21 (2009).
66. William, E. S., McNaughton, B. L. & Gothard, K. M. An information-theoretic approach to deciphering the hippocampal code. *Advances in Neural Information Processing Systems*, 1030–1037 (1992).
67. Cacucci, F., Lever, C., Wills, T. J., Burgess, N. & O'Keefe, J. Theta-modulated place-by-direction cells in the hippocampal formation in the rat. *J. Neurosci.* **24**, 8265–8277 (2004).
68. Burgess, N., Cacucci, F., Lever, C. & O'Keefe, J. Characterizing multiple independent behavioral correlates of cell firing in freely moving animals. *Hippocampus* **15**, 149–153 (2005).
69. Zhang, K., Ginzburg, I., McNaughton, B. L. & Sejnowski, T. J. Interpreting neuronal population activity by reconstruction: unified framework with application to hippocampal place cells. *J. Neurophysiol.* **79**, 1017–1044 (1998).
70. Ethan, T. & Lex, K. mouse. *Zenodo*. https://doi.org/10.5281/zenodo.3925901 (2019).

Acknowledgements

This work was funded by the Ministry of Science and Technology of China STI 2030-Major Projects (2022ZD0206700; C.M.), the Qidong-SLS Innovation Fund (2023002029 and 2020001540; C.M.), the Space Brain Project from the Lingang Laboratory, Grant No. LG-TKN-202204-01 (C.M.), Science Fund for Distinguished Young Scholars in Beijing (JQ23023; C.M.), Chinese Government Foreign Expert Project for Emilio Kropff (G2022101003L; C.M.), and PICT-2019-2596 grant from the Science Ministry of Argentina (E.K.). We are grateful for the assistance with imaging and histology provided by the National Center for Protein Sciences at Peking University in Beijing, China. We thank scidraw.io for the mouse schematic.

Author contributions

R.L., J.H. and C.M. designed the research, R.L., J.H., X.Z., S.W., Y.Y., H.C. and K.G. collected the data, R.L., J.H., E.K. and C.M. analyzed the data, C.M. and E.K. supervised the project, R.L., J.H., E.K. and C.M. wrote the paper with input from all authors.

Competing interests

The authors declare no competing interests.

Additional information

Supplementary information The online version contains supplementary material available at https://doi.org/10.1038/s41467-026-70289-3.

Correspondence and requests for materials should be addressed to Emilio Kropff or Chenglin Miao.

Peer review information *Nature Communications* thanks the anonymous reviewer(s) for their contribution to the peer review of this work. A peer review file is available.

Reprints and permissions information is available at http://www.nature.com/reprints

Publisher's note Springer Nature remains neutral with regard to jurisdictional claims in published maps and institutional affiliations.

Open Access This article is licensed under a Creative Commons Attribution-NonCommercial-NoDerivatives 4.0 International License, which permits any non-commercial use, sharing, distribution and reproduction in any medium or format, as long as you give appropriate credit to the original author(s) and the source, provide a link to the Creative Commons licence, and indicate if you modified the licensed material. You do not have permission under this licence to share adapted material derived from this article or parts of it. The images or other third party material in this article are included in the article's Creative Commons licence, unless indicated otherwise in a credit line to the material. If material is not included in the article's Creative Commons licence and your intended use is not permitted by statutory regulation or exceeds the permitted use, you will need to obtain permission directly from the copyright holder. To view a copy of this licence, visit http://creativecommons.org/licenses/by-nc-nd/4.0/.

© The Author(s) 2026